Advances in Science and Technology Research Journal

Advances in Science and Technology Research Journal, 2026, 20(10), 435–450
https://doi.org/10.12913/22998624/224753
ISSN 2299-8624, License CC-BY 4.0

Received: 2026.06.08
Accepted: 2026.07.18
Published: 2026.09.01

Modeling of casting processes using a multi-domain finite element method approach: Shrinkage cavity formation

Grzegorz Samołyk[1]

[1] Mechanical Engineering Faculty, Lublin University of Technology, ul. Nadbystrzycka 36, Lublin, Poland
E-mail: g.samolyk@pollub.pl

ABSTRACT

The accurate prediction of shrinkage defects remains a major challenge in the numerical modeling of casting processes. Many existing FEM-based casting models rely on node-based linear expansion coefficients or density approximations to simulate volumetric changes during solidification. In contrast, widely used commercial casting packages often employ FDM/FVM- or VOF-based strategies. The present paper therefore focuses on an element-based FEM formulation that calculates volume changes directly from temperature-dependent density variations and extends the analysis to a multi-domain casting–mold system. This paper presents an element-based numerical methodology that calculates volume changes directly from temperature-dependent density variations. The proposed FEM framework adopts a multi-domain approach, encompassing both the casting and the molds. The solidification model employs a multi-step iterative correction algorithm: an initial heat conduction analysis is followed by an enthalpy-based latent heat correction, with element statuses identified through a tagging system. By updating density values at the element level, the method provides a physically consistent representation of the mass-volume balance throughout the cooling process. Heat transfer between the casting and the mold domains is modeled using the fourth-kind boundary condition. The validity of this approach is demonstrated through a comparative study of a lead (Pb) ingot, where the predicted shrinkage cavity geometry is benchmarked against experimental results, supported by indirect temperature measurements. The FEM approach described herein has been fully implemented in the author's proprietary software.

Keywords: casting process, solidification, FEM, shrinkage cavity, boundary conditions.

INTRODUCTION

Numerical modeling has become an indispensable tool in modern manufacturing technology, particularly in processes governed by coupled thermal, mechanical, and phase-transformation phenomena. It facilitates the optimization of casting processes, leading to reduced production costs and shortened product development cycles. However, the analysis of casting is inherently complex, encompassing diverse stages such as mold filling, phase transitions – most notably solidification – and the subsequent cooling of the solid phase. These stages are governed by fundamentally different physical principles and require distinct mathematical models. This complexity arises primarily from the radical changes in the material's rheological and thermophysical properties during its transition from a liquid state to a solid crystalline structure.

Historically, numerical simulations of casting processes have evolved from simple finite difference methods (FDM) to more versatile finite element methods (FEM) [1]. In general, these methods provide the precision required for the analysis of geometrically complex castings. A notable example is the numerical simulation of a turbocharger housing performed by Lei [2]. Similarly, Campos Neto [3] analyzed the die-casting process for an aluminum housing, focusing on the wear of steel molds. In both instances, the simulations were performed using commercial FEM

software, divided into stages that mirrored the complete technological process with the primary objective of predicting casting defects.

However, such simulations often require enormous computational resources, are time-consuming, and can suffer from numerical instability. Furthermore, commercial software packages are strictly engineering-oriented and represent a significant financial investment. Consequently, the development of more accessible, specialized numerical models remains highly relevant for both practical applications and scientific research. One such example is the Generalized Finite Difference Method developed by Dobravec [4], optimized for specific purposes, such as analyzing dendritic crystallization while eliminating anisotropy – a feature often treated as standard in commercial FEM codes. Another example of continuous progress in FEM is the work of Węgrzyn-Skrzypczak [5], which introduces a more stable FEM formulation utilizing the Petrov-Galerkin method. This approach yields heat transfer equations incorporating a convective term, which are particularly well-suited for the analysis of the crystallization process.

The equations governing heat transfer and mass balance during solidification are not limited to casting processes. They are inherently universal, playing a critical role in various industrial applications, including welding, heat treatment, and laser additive manufacturing [6, 7]. This versatility was effectively demonstrated by Chaimano [6], who utilized a proprietary electro-thermo-mechanical FEM model to analyze welding processes. A significant conclusion arising from such research is that non-commercial FEM applications offer a level of flexibility and extensibility that facilitates the seamless integration of new physical phenomena and advanced analytical capabilities.

Research in the field of solidification modeling is generally bifurcated into two distinct trends. The first trend is rooted in metallurgical physics, focusing on the fundamental aspects of phase transformations, including grain growth kinetics and dendrite morphology at the microscale [4, 8]. This research is not limited to casting but encompasses all manufacturing processes involving crystallization [7]. The second trend is primarily technological, aiming to predict casting defects on a macroscopic scale [1, 2, 9] as well as the final mechanical properties of the solidified material [10, 11]. The overarching objective of this line of research is to improve the efficiency of industrial production. A notable example is the work by Jia et al. [12], which investigates the solidification of magnesium alloy ingots.

Within the technological scope, predicting the formation of shrinkage cavities remains a significant engineering challenge. Many existing predictive models utilize a nodal strategy, where volumetric changes are estimated using the linear thermal expansion coefficient – or, in some cases, density variations – interpolated at the nodes of the finite element mesh [1, 11, 13]. For instance, Skrzypczak [14, 15] proposed a procedure for calculating shrinkage cavities by considering isolated volumes of the liquid phase interpolated to the nodes. Similarly, Węgrzyn-Skrzypczak [13, 16] modeled solidification shrinkage by utilizing spherical grains within cubic cells, with element volumes still mapped to the nodes. While the nodal approach is efficient for certain applications, it often struggles to maintain mass conservation in regions characterized by steep temperature gradients or abrupt phase transitions, potentially compromising the accuracy of the predicted shrinkage cavity morphology [17]. Furthermore, the inherent complexity of some existing models can paradoxically diminish the reliability of the numerical results.

It is important to note that modern commercial software suites for casting process simulation, such as MagmaSoft or FlowCast, utilize more advanced structural discretization techniques [18, 19]. Unlike classical FEM, these systems are predominantly based on FVM or FDM employing Cartesian grids. A key feature of their free-surface modeling, which encompasses shrinkage cavity formation, is the compensation for volumetric shrinkage via the VOF algorithm [20]. This approach enables continuous tracking of metal volume fluctuations by calculating the cell fill factor, ensuring that all cells remain active throughout the calculation process. However, these programs are typically limited to modeling a single domain – the casting itself – and rely on simplified boundary conditions.

In addition to classical physics-based casting models, recent research in mechanical engineering has increasingly explored data-driven, fuzzy and machine-learning-based procedures for parameter estimation, model calibration and uncertainty reduction. Recent research in the field of mechanical engineering has demonstrated that numerical models need not be limited to

deterministic heat-transfer calculations. They are increasingly being combined with procedures based on intelligent, fuzzy, and machine-learning-based procedures, especially when the modeled process involves strong nonlinearities, uncertain parameters, or quantities that are difficult to measure experimentally. Examples of this include the work of He [21], Precup et al. [22], and Milićević et al. [23]. For example, hybrid machine learning has already been used to improve the mechanical properties of additively manufactured objects, demonstrating that data-driven approaches can complement classical numerical models in production-oriented research [23]. Nevertheless, in casting simulation, the accuracy of shrinkage defect prediction still strongly depends on the physical consistency of heat-transfer modeling, phase-front tracking, density variation, and free-surface evolution. In the present study, these approaches are not used as a replacement for the FEM formulation, but they indicate possible future extensions of the proposed multi-domain framework.

This paper proposes an alternative methodology for modeling volume changes during phase transformations within an FEM framework, with specific focus on shrinkage cavity formation. Departing from conventional nodal-based strategies, this approach considers density variation as a direct function of temperature, with calculations performed at the element level. A multi-step iterative algorithm is introduced: it involves solving the heat conduction equation, applying a latent heat correction based on enthalpy, and subsequently compensating for density variations through the systematic removal of selected elements. This approach offers a more physically consistent representation of mass and volume balance, facilitates clearer phase identification, and ensures a stable tracking of the casting's free surface. Furthermore, the methodology is both simple and intuitive. Unlike models limited to the casting domain, this approach incorporates the entire system – including the surrounding molds – by applying fourth-kind boundary conditions to calculate heat transfer at all domain interfaces. The proposed methodology should also be understood as part of broader efforts aimed at developing specialized computational tools for applications in mechanical engineering. Although commercial simulation packages offer advanced functionality, their internal algorithms and simplifications are often inaccessible to the user. In contrast, the proprietary implementation of the FEM allows for direct control over, for example, the formulation of volume changes at the element level, density updates, latent heat correction, and the implementation of the aforementioned boundary conditions.

The article also presents a validation of this methodology by comparing numerical simulations, performed using a proprietary FEM code, with experimental results from a cast lead (Pb) ingot. The analysis includes a comparison of temperature transients at selected control points and the final geometry of the shrinkage funnel. The results demonstrate that the proposed element-based strategy effectively captures the solidification dynamics, providing an accurate representation of both shrinkage cavity formation and free-surface evolution.

Thus, to summarize, the main novelty of the study lies in: (i) calculating volumetric shrinkage at the element level through temperature-dependent density updates; (ii) applying a multi-domain FEM model that includes the casting, mold, molding sand and surrounding thermal environment; and (iii) validating the predicted shrinkage cavity morphology against an experimental Pb ingot supported by indirect temperature measurements.

NUMERICAL METHODOLOGY AND SOFTWARE ARCHITECTURE

Basic theory of axisymmetric thermal-mechanics FEM

The analysis of unsteady heat conduction is governed by Fourier's law [24], which, for axisymmetric problems, is expressed by the following partial differential equation:

$$\frac{1}{r}\frac{\partial}{\partial r}\left[r\lambda\frac{\partial T(r,z,t)}{\partial r}\right]+\frac{\partial}{\partial z}\left[\lambda\frac{\partial T(r,z,t)}{\partial z}\right]+ \\ +Q(r,z,t)=c\rho(T)\frac{\partial T(r,z,t)}{\partial t} \quad (1)$$

where: λ, c, and ρ denote the thermal conductivity, specific heat capacity, and density of the material, respectively. T represents the temperature at a specific time t and at a given spatial point defined by the coordinates r (radial direction) and z (axial direction).

Applying the Galerkin weighted residual method [24, 25] and utilizing a finite difference

scheme for the temporal discretization of the temperature derivative, the governing partial differential equation is transformed into a system of linear algebraic equations:

$$[K] \cdot \{T\}_t + \frac{1}{\Delta t} \cdot [P] \cdot (\{T\}_t - \{T\}_{t-\Delta t}) = \{W\} \quad (2)$$

In this discretized system, [K] and [P] represent the global thermal conductivity and heat capacity matrices, respectively. The vectors $\{T\}_t$ and $\{T\}_{t-\Delta t}$ denote the nodal temperatures at the current and previous time steps. Furthermore, {W} represents the vector of free terms, accounting for internal heat sources and boundary conditions, while Δt corresponds to the time step.

Equation 2 assumes its final form after incorporating the heat source contributions at the element level and the boundary conditions defined at the domain interfaces. Specifically, by incorporating the Robin boundary condition (commonly referred to as the third-kind condition), the governing system is expressed as Equation 3. Conversely, when accounting for the continuity condition at the interfaces (the fourth-kind boundary condition), the system is represented by Equation 4.

$$\left([K] + [B]_1^{(III)} + \frac{1}{\Delta t}[P]\right) \cdot \{T\}_t = \\ = \frac{1}{\Delta t}[P] \cdot \{T\}_{t-\Delta t} + \{Z\} + \{B\}_2^{(III)} \quad (3)$$

$$\left([K] + [B]_1^{(IV)} + [B]_2^{(IV)} + \frac{1}{\Delta t}[P]\right) \cdot \{T\}_t = \\ = \frac{1}{\Delta t}[P] \cdot \{T\}_{t-\Delta t} + \{Z\} \quad (4)$$

In the formulations above, $[B]_1^{(III)}$ and $\{B\}_2^{(III)}$ represent the matrix and load vector associated with convective heat flux from the domain boundary to the ambient environment at a constant temperature (Robin boundary condition). Conversely, $[B]_1^{(IV)}$ and $[B]_2^{(IV)}$ denote the matrices accounting for the heat flux between two adjacent discrete regions, incorporating an interface resistance representing a conventional gas gap (fourth-kind boundary condition). Numerically, this condition is implemented by enforcing a heat balance between adjacent elements e_1 and e_2, which belong to different domains. The matrices $[B]_1^{(IV)}$ and $[B]_2^{(IV)}$ are derived by solving the following heat balance equation:

$$\frac{1}{R}\int_{e_1} \{T_1\} d\Gamma_1 = \frac{1}{R}\int_{e_2} \{T_2\} d\Gamma_2 \quad (5)$$

Here, R represents the thermal resistance of the gas gap, which depends on the gap width and the thermal conductivity of the medium. The fourth-kind condition is utilized specifically when the mold is also discretized using finite elements. It is also worth noting that the general formulation allows for the representation of other boundary conditions. If the matrix $[B]_1^{(III)}$ in Equation 3 is set to zero, the vector $\{B\}_2^{(III)}$ represents the prescribed heat flux density, corresponding to the Neumann boundary condition (second-kind condition). A special case occurs when this heat flux is zero, representing an adiabatic boundary condition, which is typically applied along the axis of symmetry.

Upon completion of solidification, the solid phase continues to cool, leading to cooling shrinkage and the development of thermal stresses. The proposed model employs a quasi-static approach, utilizing a linear elastic (Hookean) model for the molds and an elastic-plastic model for the castings, rather than a full viscoelastic formulation. This quasi-static approach simplifies the analysis by considering incremental deformation at each computational step. The solution is derived from the differential equation of equilibrium, which, for axisymmetric geometries, is expressed as follows:

$$\frac{\partial \sigma_r}{\partial r} + \frac{\partial \sigma_{zr}}{\partial z} + \frac{(\sigma_r - \sigma_\theta)}{r} = 0 \\ \frac{\partial \sigma_{rz}}{\partial r} + \frac{\partial \sigma_z}{\partial z} + \frac{\sigma_{rz}}{r} = 0 \quad (6)$$

The constitutive relationship governing the quasi-static analysis, which accounts for thermal shrinkage, is based on the generalized Hooke's law. For an isotropic material, this relationship is expressed as:

$$\{\Delta\sigma\} = [D] \cdot (\{\Delta\varepsilon\} - \{\Delta\varepsilon_0\}) \quad (7)$$

where: {Δσ} and {Δε}−represent the stress and strain increment vectors, respectively; [D] denotes the elasticity matrix for the axisymmetric state, where both Young's modulus (E) and Poisson's ratio (ν) are defined as temperature-dependent functions. The vector $\{\Delta\varepsilon_0\}$−represents the strain increment vector arising from volumetric shrinkage, calculated based on the density variation over the time step Δt, and is defined as:

$$\{\Delta\varepsilon_0\} = \frac{\rho(T)_t - \rho(T)_{t-\Delta t}}{3\rho(T)_{t-\Delta t}} \cdot \{1,1,1,0\}^T \quad (8)$$

For the casting domain, the material behavior is modeled using an elastic-plastic framework, where the total strain increment $\{\Delta\varepsilon\}$ is decomposed into elastic and plastic components. To determine the plastic strain, the iterative radial return mapping (RRM) algorithm [25] is employed. This procedure verifies whether the stress increment $\{\Delta\sigma\}$ exceeds the yield strength of the material; if the yield criterion is met, a plastic strain increment is introduced. It should be emphasized that incorporating mechanical analysis significantly improves the physical accuracy of the model. Specifically, it enables the constant gap resistance R in Equation 5 to be replaced by a variable, displacement-dependent function that accounts for dynamic contact conditions and node displacements between the casting and the mold. Thus, the mechanical model not only determines thermal stress in the already solidified domain but also improves the prediction of cooling shrinkage.

Author's program architecture

The proposed mathematical model and accompanying numerical algorithms have been implemented in a custom-developed software application, referred to as TGrid2D. This program was developed within the.NET (VB.NET) object-oriented environment using a 64-bit architecture, which enables the processing of large-scale finite element meshes. Furthermore, the program's modular design ensures a flexible architecture and facilitates the integration of additional mathematical models.

The TGrid2D application consists of three independent, communicating subprograms. The pre- and post-processor modules are developed within a graphical user interface (GUI) environment, whereas the solver is implemented as a console application to ensure computational stability and maximize the utilization of system processing power. A block diagram of the application is presented in Figure 1, which illustrates the workflow within the pre-processor module. A critical final step involves finite element mesh optimization and node reordering. These tasks are performed using element shape correction algorithms [26] and the Reverse Cuthill-McKee (RCM) algorithm [27, 28], respectively. The intermediate objective is to obtain a sparse matrix, while the ultimate goal is to maximize solver efficiency. Beyond these three primary modules, the application includes databases of materials – covering casting and molding materials, as well as ambient air properties – and defined boundary conditions. The author has opted against commercial packages in favor of implementing proprietary, optimized algorithms and custom data structures.

Following the definition of the numerical task within the pre-processor, an input file is generated and transmitted to the core module – the solver – the block diagram of which is presented in Figure 2. The simulation is executed through several key stages, assuming a constant time step Δt. Each iteration begins by defining the set of elements involved in the computation. This set comprises elements belonging to both the casting and mold domains, while excluding elements designated with the 'air' tag, i.e., those representing the shrinkage cavity volume. Initially, the temperature field is calculated. To this end, the stiffness matrix and the vector of free terms are assembled, incorporating boundary conditions and potential heat sources. This assembly process encompasses all elements within the defined set. Upon solving Equation 3 or 4, the temperature field is corrected; this method, along with the algorithm for calculating solidification shrinkage, is elaborated in the subsequent subsections. The final stage involves determining the cooling shrinkage, specifically for the subset of elements assigned the 'solid' tag. These calculations are performed using an elastic or elastic-plastic material model.

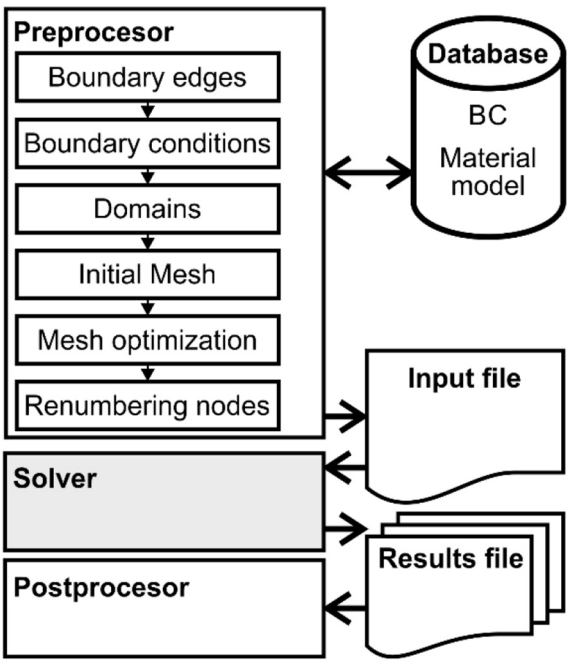

Figure 1. General block diagram of the proprietary TGrid2D software architecture

It should also be emphasized that element subsets are generated at each computational step. Each subset is treated as an integral domain to which appropriate material properties and governing equations are assigned. Thermal and mechanical boundary conditions are defined at the interfaces of these regions, where necessary. Furthermore, these conditions may result from interactions between specific regions. Elements within these subsets are assigned categorical tags; for instance, elements representing the casting domain are classified as 'liquid,' 'solid,' or 'air,' corresponding to the liquid phase, solid phase, and void space (e.g., shrinkage cavity, funnel etc.), respectively. Based on this identification, the algorithm constructs appropriate domains with defined properties. The multi-domain approach allows for the extraction of liquid regions separated by solid regions, making it possible to predict the formation of independent shrinkage cavities throughout the entire casting volume.

From a software engineering perspective, the modular structure of TGrid2D aligns with current trends in digital mechanical engineering systems. As demonstrated by the work of Li et al. [29], there is a trend toward increasingly integrating simulation, data processing, monitoring, and decision support modules into unified computational environments. Although this study focuses on offline FEM simulation, the adopted modular architecture provides a suitable foundation for future integration with experimental databases, real-time measurements, or automated calibration procedures [30].

Enthalpy-based temperature correction

A significant challenge in modeling the solidification process is tracking the crystallization front, as it represents a dynamic, narrow region characterized by a point heat source. This problem was addressed using a two-step iterative correction algorithm. Initially, applying the fundamental Equation 3 or 4, the base temperature field is determined for the entire set of elements representing the casting and the mold (if discretized). For the casting domain, uniform volumetric heat capacity is assumed across the entire region. The heat capacity matrix [P] is computed using constant values for specific heat capacity c and density ρ, corresponding to the liquidus temperature T_L (or the pouring temperature, where applicable). Conversely, the thermal conductivity matrix [K] is computed using the thermal conductivity coefficient λ at the initial temperature of the current time step, averaged over the element. In the second stage (as illustrated in Figure 2), the initial temperature T_g within the casting domain is corrected. This requires an indirect a posteriori adjustment of the capacitance matrix [P], while simultaneously accounting for the latent heat of fusion L_v. This is achieved by introducing the effective heat capacity C_{eff}. This parameter

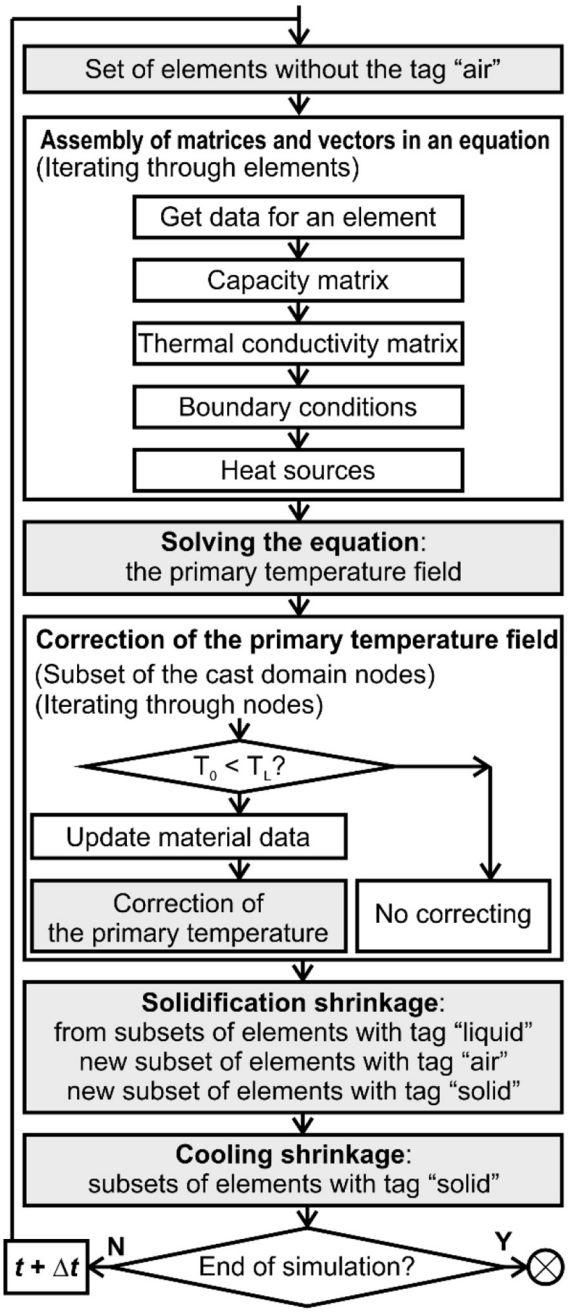

Figure 2. Detailed workflow of the Solver module, outlining the iterative thermal analysis, latent heat correction, and the sequential calculation of solidification and cooling-induced shrinkage

accounts for the change in volumetric heat capacity over the temperature range from the initial T_0 to T_g, as well as the solidification process occurring between the liquidus T_L and solidus T_S temperatures. Consequently, the effective heat capacity is defined as:

$$C_{eff} = \frac{1}{2}(c_0 + c_g)(\rho_0 + \rho_g) + \frac{\rho_s L_v}{T_L - T_S} \quad (9)$$

It can now be assumed that the enthalpy change calculated by the solver in the first stage must equal the actual enthalpy change dictated by the physics of the solidification process. Consequently, the energy derived from the Fourier heat conduction equation (excluding the latent heat of solidification) must be balanced by the total energy required for the metal to transition from the initial temperature T_0 to the actual temperature T_1, accounting for the solidification process. This energy balance can be expressed as follows:

$$\Delta H_{solver} = \Delta H_{real} \quad (10)$$

$$(c_L\rho_L)(T_0 - T_g) = \int_{T_0}^{T_1} C(T)dT \quad (11)$$

where: T_0, T_g, and T_1 denote the initial temperature, the temperature calculated in the first stage, and the actual (corrected) temperature, respectively, which accounts for both the variable heat capacity and the latent heat of solidification.

Expanding the heat balance Equation 11 yields the following:

$$(c_L\rho_L)(T_0 - T_g) = (c_L\rho_L)(T_0 - T_L) + \\ + C_{eff}(T_L - T_S) + (c_S\rho_S)(T_S - T_1) \quad (12)$$

from which the corrected temperature T_1 is determined as follows:

$$T_1 = T_S + \frac{C_{eff}}{(c_s\rho_s)}(T_L - T_S) - \frac{(c_L\rho_L)}{(c_s\rho_s)}(T_L - T_g) \quad (13)$$

Equation 12 is applicable under the condition $T_0 > T_L$ and $T_g < T_S$. However, for other thermal conditions, Equation 12 must be modified accordingly. Specifically, only the phase transitions occurring during cooling within the respective temperature range should be considered. For instance, when $T_0 < T_L$ and $T_g < T_S$, the energy balance is expressed by Equation 14, whereas for the case where $T_0 < T_S$ and $T_g < T_S$, Equation 15 applies.

$$(c_L\rho_L)(T_0 - T_g) = +C_{eff}(T_0 - T_S) + \\ + (c_S\rho_S)(T_S - T_1) \quad (14)$$

$$(c_L\rho_L)(T_0 - T_g) = (c_S\rho_S)(T_0 - T_1) \quad (15)$$

Numerical simulation of shrinkage cavity

The calculation of solidification shrinkage is based on the volumetric change of individual elements. This approach is not only intuitive but also accurately reflects the physical nature of the modeled process, while facilitating the implementation of a computationally efficient algorithm. The element volume change, ΔV_s, representing shrinkage during solidification, is calculated based on the variation in material density as follows:

$$\Delta V_s = V_e\left(1 - \frac{\rho(T_L)}{\rho(T_S)}\right) \quad (16)$$

where: V_e is the initial volume of the element at the beginning of the simulation, and $\rho(T_L)$ and $\rho(T_S)$ denote the material density at the liquidus and solidus temperatures, respectively.

The algorithm is based on generating subsets of elements representing the unsolidified region or the region currently undergoing solidification. These elements are sorted by coordinate, following the assumed direction of gravity. Subsequently, based on the initial and final temperatures within a given computational step, elements in which the solidification process has just concluded are identified. Their state tags are updated, and the shrinkage volume is calculated using Equation 16. Upon summing all incremental shrinkage volumes, the resulting total is distributed among the elements with the highest coordinate within the given subset that are still in the liquid phase. If the shrinkage volume equals the total volume of a specific element, its tag is updated to 'Air.' Consequently, this element represents a void – forming a shrinkage cavity (or funnel) – and is excluded from further analysis, which, for instance, allows for a reduction in the system matrix size.

Although this approach strikes a balance between mass and volume, it is nevertheless a simplified technique, distinct from a fully physics-based fluid flow simulation technique (such as the VOF method in commercial software). However, by using a multi-domain approach, this technique can also be applied to complex geometries with

isolated hot spots or enclosed liquid reservoirs. The author plans to continue developing this area.

CASE STUDY: THE INGOT MAKING PROCESS

FEM model setup

As an illustrative example of the application of the proposed multi-domain finite element method and its associated algorithms, the solidification process of a technically pure Pb1-grade lead ingot in a cylindrical steel mold was selected. The simulation was conducted over a process duration of 1200 seconds, using a time step of Δt = 0.1 s. A schematic representation of the process is shown in Figure 3, which accurately replicates the conditions of the experimental tests. The initial height of the ingot (labeled 1 in Figure 3) at the pouring temperature is H = 60 mm. The pouring temperature of the molten lead is T_{01} = 400 °C, while the ambient temperature (labeled 6) is maintained at a constant T_{∞} = 18.5 °C. The inner diameter of the steel mold (labeled 2) is D = 48.1 mm, with a wall thickness b_f = 10 mm. The mold is manufactured from hot-work tool steel and has an initial temperature T_{02} = 18.5 °C. The mold is embedded in molding sand (labeled 3), which rests on a steel plate (labeled 5). The thickness of the molding sand layer directly beneath the ingot is h_m = 22 mm. An additional domain included in the model is the air transition zone (labeled 4) with a width of b_a = 11 mm. Two virtual sensors, S_3 and S_4, were defined to represent thermocouples recording the temperature on the outer surface of the mold, matching their placement in the experimental setup. Two additional sensors, S_1 and S_2, were positioned within the molding sand directly below the ingot base. These sensor locations were selected because direct temperature measurement inside the molten lead or within the steel mold wall is physically impossible during the casting process.

The regions labeled 1 through 4 (Figure 3) were discretized into a total of 3000 triangular elements (1772 nodes). An adiabatic boundary condition (q = 0 W/m^2) was applied along the axis of symmetry. The free surface of the model, in contact with the environment (labeled 6), was defined using a third-kind boundary condition (Robin boundary condition), where the heat flux is governed by Newton's law of cooling. The

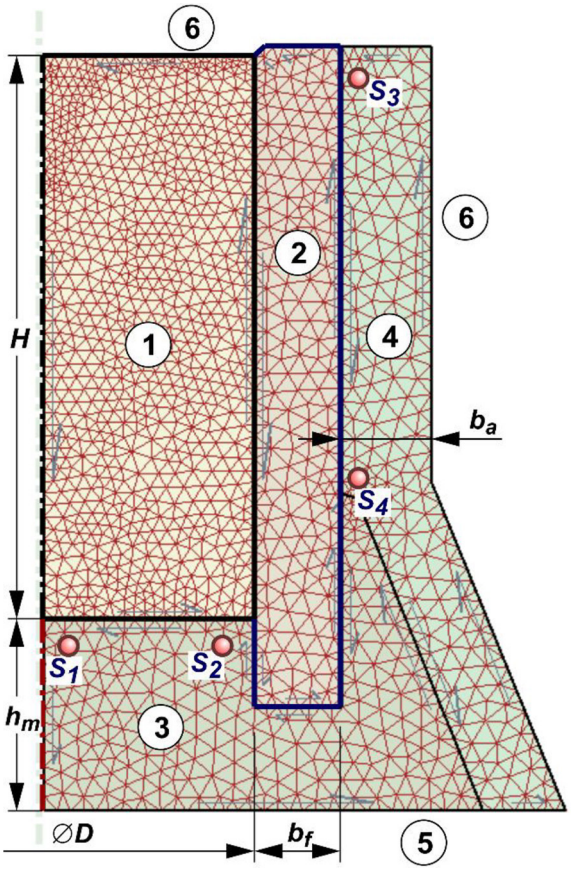

Figure 3. FEM model of the solidification process: 1 – lead ingot, 2 – steel mold, 3 – molding sand, 4 – air transition zone, 5 – steel plate, 6 – ambient air

effective heat transfer coefficient, α, was defined as a function of the surface temperature. Specifically, it was assumed that at T = 18.5 °C, α = 20 W/(m^{2}K), whereas at $T \geq$ 327 °C, α = 30 W/(m^{2}K). Additionally, at the interface between the molding sand (labeled 3) and the steel plate (labeled 5), a similar boundary condition was applied with a constant heat transfer coefficient of α = 1000 W/(m^{2}K).

Fourth-kind boundary conditions were applied at the interfaces between discrete regions, in accordance with Equation 5. In certain cases, a variable resistance R was employed to represent the dynamics of the solidification and cooling processes. At the interface between the ingot (labeled 1) and the molding sand (labeled 3), the thermal conductivity of the gas gap was assumed to be λ = 0.038 W/(mK), with the gap thickness g being a function of the ingot temperature. When the ingot is in the liquid phase ($T \geq$ 327 °C), the gap thickness is set to g = 0.06 mm; however, following lead solidification ($T <$ 327 °C), it increases to g = 0.14 mm. These values account for the physical

nature of the process and the surface characteristics of the molding sand. A similar approach was implemented at the side interface between the lead ingot (object 1) and the steel mold (object 2), where the gap thickness was set to g = 0.08 mm and g = 0.25 mm, respectively, reflecting the surface topography of the metal mold and its orientation relative to gravity. Conversely, a constant gap thickness of g = 0.07 mm was adopted for the boundary between the steel mold (labeled 2) and the molding sand (labeled 3).

In the case of the boundaries between the steel mold (labeled 2), the molding sand (labeled 3), and the air transition zone (labeled 4), specifying a precise gas gap value is less critical than for the aforementioned interfaces. Here, the thickness g is treated as a nominal, discrete air layer. Consequently, the model assumes a priori that g = 0.1 mm, a value that ensures computational stability and minimizes numerical errors.

Figure 4 summarizes the essential material properties of technically pure lead utilized in the FEM simulation. All three parameters are temperature-dependent, enabling a comprehensive representation of the physical phenomena occurring during solidification and subsequent cooling. Supplementary data include the latent heat of fusion, $L = 23.03 \times 10^3$ J/kg, and the characteristic phase transition temperatures. Although a pure metal was employed, the simulation utilizes a solidification model operating over a narrow temperature interval; consequently, a solidus-liquidus range was defined, specifically T_S = 327.5 °C and T_L = 327.6 °C.

Figures 5 and 6 illustrate the material properties for the metal mold (hot-work tool steel) and the molding sand, respectively. For the molding sand, a constant density of $\rho = 2 \times 10^3$ kg/m^3 was assumed across the entire temperature range. Notably, neither latent heat nor phase transition temperatures are defined for these two domains (labeled 2 and 3), as phase transformations are not calculated for these materials.

The thermophysical data used in this study were selected from established sources [31, 32] and the CastFlow database. The data from CastFlow are taken from its internal materials database (2023 version, available at the Lublin University of Technology). Regarding the interfacial thermal resistance and gas-gap thickness, the model adopts a conservative approach, utilizing values that account for surface roughness and the gap evolution during solidification, as commonly

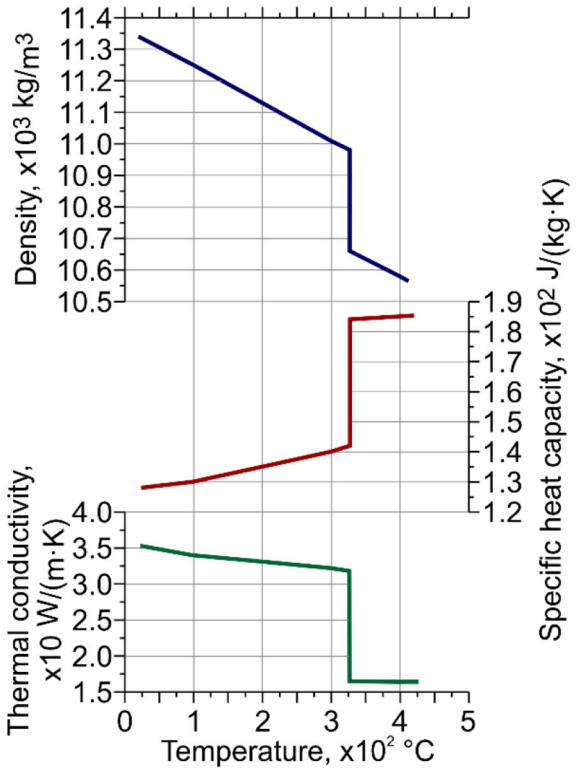

Figure 4. Essential thermophysical properties of technically pure lead (Pb1-grade) as a function of temperature: thermal conductivity $\lambda(T)$, specific heat capacity $c(T)$, and density $\rho(T)$

practiced in the modeling of non-ferrous metal casting [33]. This approach ensures physical consistency when representing the thermal contact state between the casting and the mold, effectively capturing the heat-transfer limitations inherent in metal dies and sand molds.

Experimental setup

The experimental setup illustrated in Figure 7 was utilized to validate the proposed multi-domain FEM application and the implemented algorithm for shrinkage cavity (funnel) prediction. Its geometric configuration corresponds to the model previously defined in Figure 3. The experimental apparatus comprises a steel mold embedded in molding sand (Figure 7b) and a high-precision data acquisition system (Figure 7a). The latter consists of a Testo 176T4 four-channel data logger connected to four K-type thermocouples, featuring an operating range of -199 °C to 1000 °C. The measurement uncertainty of this system complies with the EN 60584-1 standard, with a declared accuracy of ±0.5%. The molten lead was poured into the mold at a temperature of 400 ±5 °C (Figure 7c).

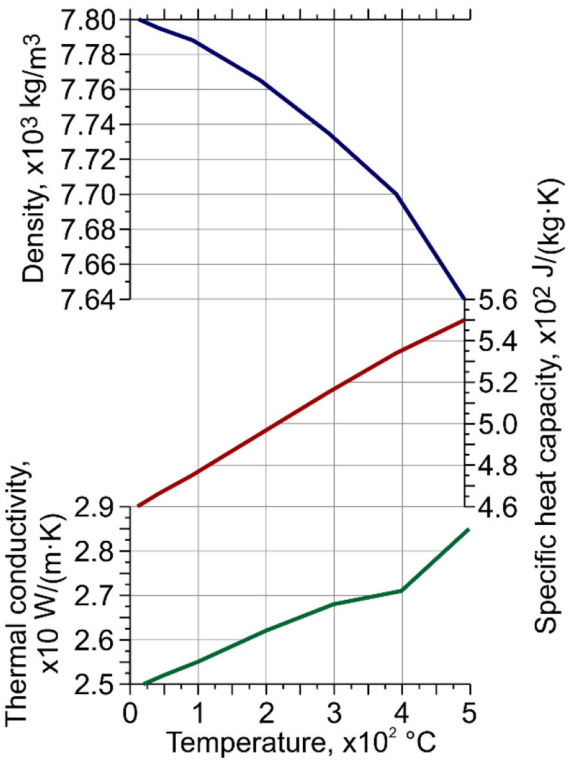

Figure 5. Essential thermophysical properties of hot-work tool steel (mold domain 2) as a function of temperature

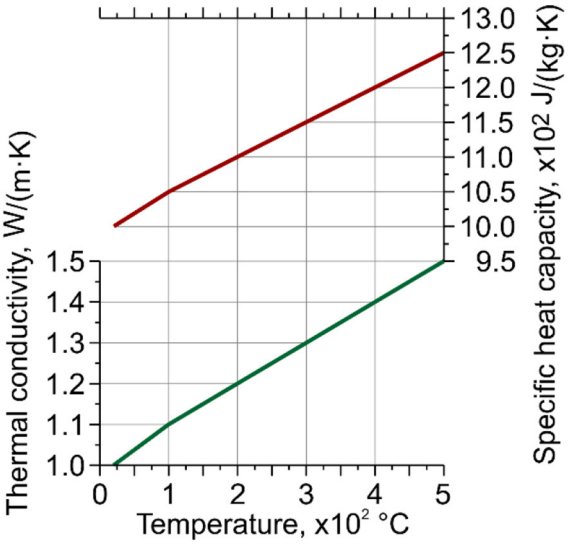

Figure 6. Essential thermophysical properties of molding sand (domain 3) as a function of temperature; sand density is assumed constant ($\rho = 2 \times 10^3$ kg/m³)

Validating solidification process models is inherently challenging because the most relevant thermal and geometric phenomena occur inside a high-temperature, rapidly changing, and physically inaccessible domain. The most straightforward validation approach is therefore the comparison of the final state of the casting, since the ultimate geometry of the shrinkage cavity or funnel is a direct consequence of the complete thermal history of the process. Monitoring temperature dynamics provides a critical supplement to this comparison, but the selection of measurement points is constrained by the fragility of thermocouples and by the harsh casting environment. Similar difficulties are encountered in other areas of experimental mechanics, where indirect, optical, or photogrammetric measurements have been introduced to validate finite element and analytical models when direct measurement is impractical [23]. In the present study, thermocouples T1 and T2 (Figure 7b) were embedded in the molding sand at a depth of approximately 2 mm from the casting surface to provide an indirect measure of the temperature near the ingot. Thermocouples T3 and T4 were affixed to the outer surface of the metal mold to monitor mold temperature as a proxy for heat transfer from the upper regions of the ingot. In the numerical FEM model (Figure 3), these measurement points were replicated with a spatial accuracy of 1 mm.

RESULTS AND DISCUSSION

The results of the solidification process simulation are presented in Figure 8, illustrating the temperature evolution across the ingot and mold cross-sections at successive stages of the process. The brown line within the ingot region represents the isotherm corresponding to the liquid-solid phase boundary (solidus temperature). Based on the numerical results, the ingot crystallization process was completed, and a shrinkage funnel was formed after approximately 155 seconds. The subsequent phase of the process is characterized by the cooling of the ingot and the heat transfer to the surrounding mold and ambient environment.

Figures 9 and 10 present a comparison between the temperatures calculated via FEM and those recorded by thermocouples embedded in the molding sand, positioned directly beneath the ingot base. For these experimental measurements, a total uncertainty of ±4 °C was assumed. This value accounts for both the intrinsic uncertainty of the measurement system (±1.5 °C) and an additional margin of ±2.5 °C, which compensates for local inhomogeneities in the sand structure and potential positioning errors related to grain size. Such a confidence interval is consistent with

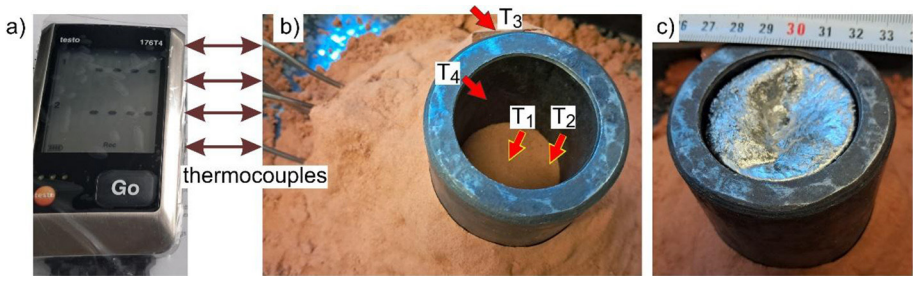

Figure 7. An experimental setup consisting of a Testo 176T4 temperature logger (a), four thermocouples, a tube-casting mold embedded in molding sand (b), and a sample ingot (c)

established standards for measurements within heterogeneous, porous media [33]. To quantitatively assess the accuracy of the numerical model, the root mean square error (RMSE) was calculated for all sensors. The obtained RMSE values were as follows: RMSE_S1 = 5.14 °C and RMSE_S2 = 4.80 °C. These values and the characteristics of the graphs suggest that the quantitative and qualitative agreement between the predicted temperature profiles and the experimental data is acceptable. It was also noted that, from approximately the 300th second of the process, the FEM-calculated temperatures are slightly higher than the experimental values. This observation indicates that further refinement of interfacial thermal resistance, gas-gap evolution, heat-transfer coefficients and thermophysical input data may improve the predictive accuracy of the model.

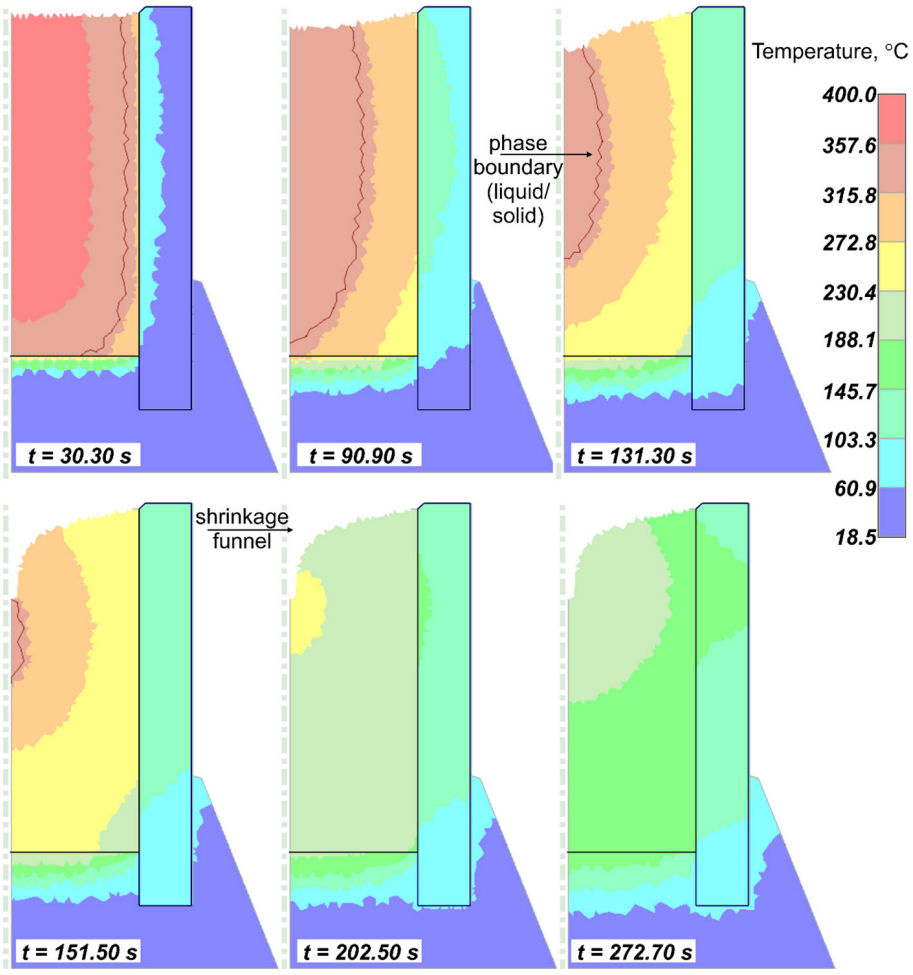

Figure 8. Temperature distribution across the ingot and mold cross-sections during selected solidification phases, including the visualization of the shrinkage funnel formation

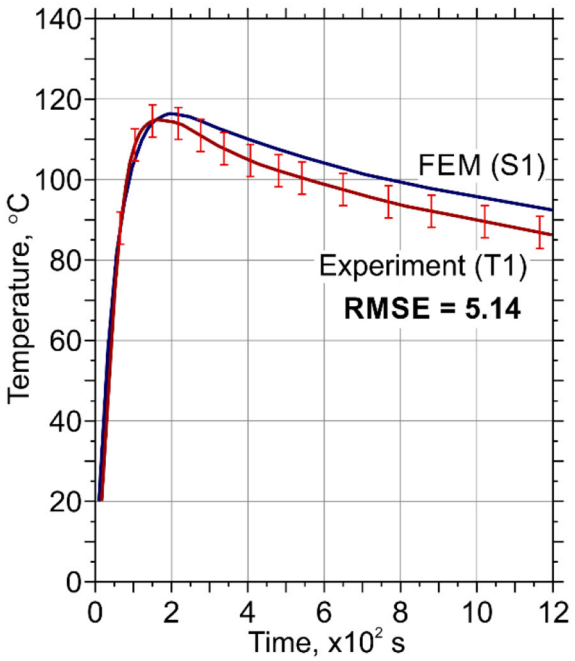

Figure 9. Comparison of the FEM-calculated temperature (virtual sensor S1) and the experimental temperature recorded by thermocouple T1 within the molding sand

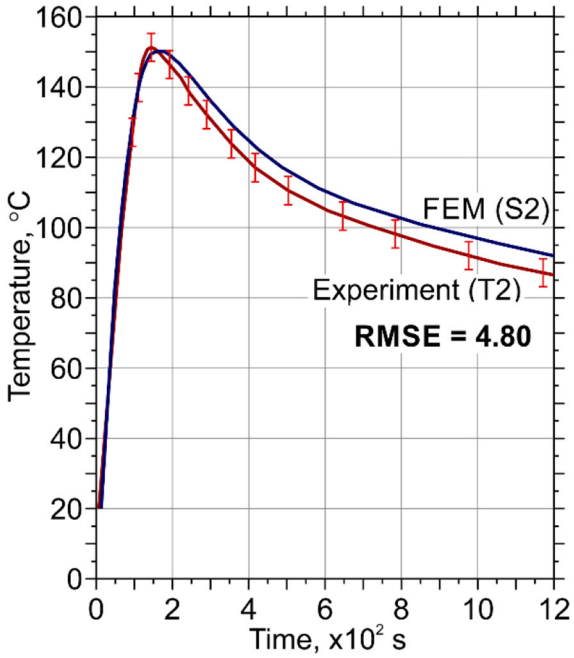

Figure 10. Comparison of the FEM-calculated temperature (virtual sensor S2) and the experimental temperature recorded by thermocouple T2 within the molding sand

The temperature measurement on the outer surface of the steel mold presents significantly higher complexity. In this instance, the estimated uncertainty is ±10 °C. This value accounts for the inherent difficulty in achieving perfect thermal contact between the thermocouple and the metal surface, as well as the sensitivity of the sensor to the surrounding environment. Specifically, the accepted margin of error compensates for the 'fin effect', where the thermocouple leads act as unintended heat dissipation paths, and for inconsistencies in local heat transfer at the contact interface. This uncertainty range addresses the challenges of precise surface temperature measurement under conditions of forced convection and steep thermal gradients. The experimental temperatures recorded on the mold surface are compared with the numerical results in Figures 11 and 12. Analogous to the previously discussed cases involving the molding sand, the quantitative and qualitative agreement between the FEM calculations and the experimental data is within acceptable limits. The RMSE values obtained for these sensors were as follows: RMSE_S3 = 3.64 °C and RMSE_S4 = 7.12 °C. A notable exception is observed for virtual sensor S3, located in the upper region of the system (Figure 3), where the calculated temperature trend deviates more distinctly from the T3 measurements. This discrepancy likely arises from the proximity of the S3 sensor to the boundary of the discrete domains. Nevertheless, as these deviations remain within the established uncertainty tolerances, it is concluded that the proposed multi-domain FEM model represents the actual solidification process and thermal distribution with sufficient accuracy, effectively accounting for the influence of the peripheral domains and mold components.

The observed discrepancies also point to a potential direction for further model improvement. One possible and interesting approach to the further development of the proprietary software could involve including, for example, a data-driven calibration layer. Such a hybrid approach is proposed in [22, 23]. Of course, such an approach will never replace the physics-based formulation of the finite element method (FEM), but it can support the estimation of uncertain parameters.

The final validation of the multi-domain FEM implementation concerns the geometric accuracy of the predicted shrinkage funnel compared to the experimental specimen. This comparison is illustrated in Figure 13. The relative difference between the calculated funnel depth and the experimental results does not exceed 12.5%, while the

transverse dimensions exhibit even higher agreement, with deviations remaining below 4%. Given the high degree of qualitative alignment, it can be concluded that the proposed shrinkage cavity calculation algorithm provides promising results for the analyzed case. Nevertheless, the observed quantitative discrepancies, particularly regarding the funnel depth, indicate that the model remains sensitive to temperature-dependent density data, interfacial thermal resistance, gas-gap thickness and heat-transfer coefficients.

The results presented above were obtained using a finite element mesh optimized in terms of element size and distribution. Specifically, the mesh density was locally increased in the region where the shrinkage cavity forms. Figure 14 illustrates the calculated shrinkage cavity shapes for three different mesh resolutions, including the average element size and standard deviation for each. Furthermore, Figure 15a displays the temperature history at a selected location (sensor 5), while Figure 15b compares the results obtained from meshes B and C by presenting the absolute temperature deviation relative to mesh A.

Based on these figures, it can be observed that mesh density variations – within a reasonable range – yield consistent shrinkage cavity morphology, indicating the numerical stability of the proposed approach. Although coarser meshes have a detectable effect on the calculated temperature fields, the results remain within an acceptable range; that is, the maximum absolute

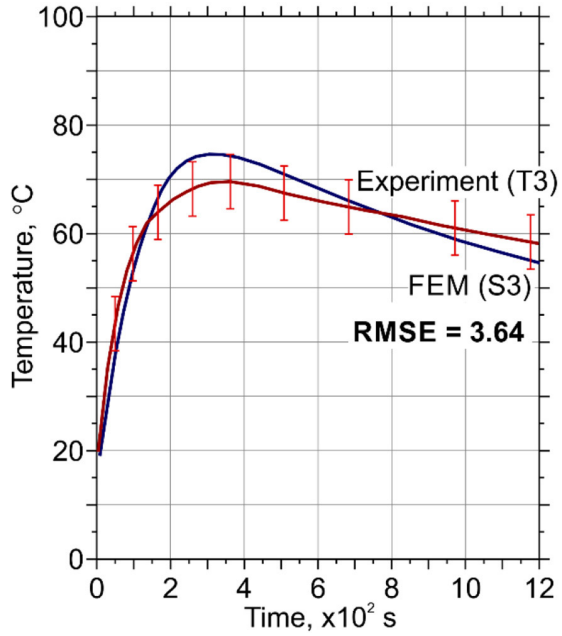

Figure 11. Comparison of the FEM-calculated temperature (virtual sensor S3) and the experimental temperature recorded by thermocouple T3 on the outer surface of the steel mold

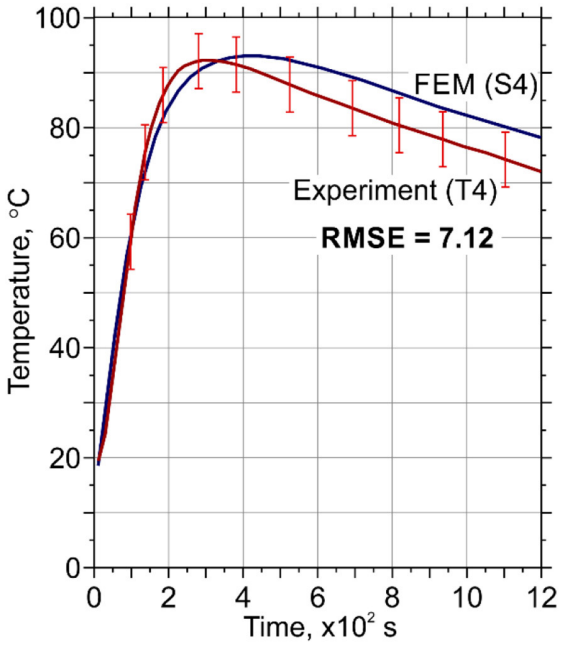

Figure 12. Comparison of the FEM-calculated temperature (virtual sensor S4) and the experimental temperature recorded by thermocouple T4 on the outer surface of the steel mold

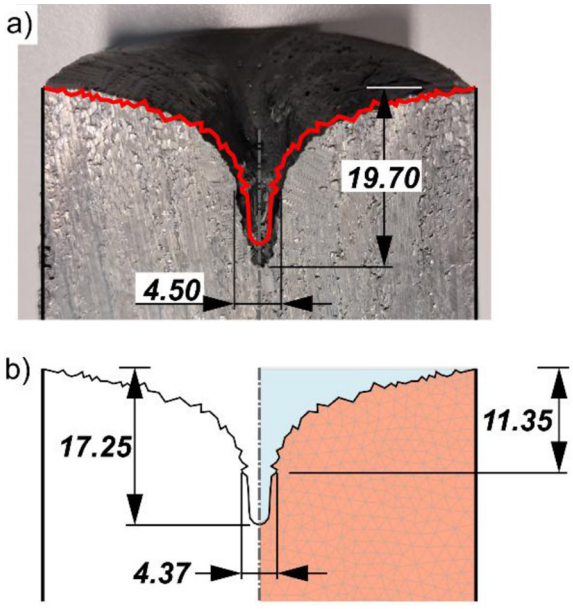

Figure 13. Comparison of the shrinkage funnel morphology: (a) experimental results obtained from a cross-sectioned ingot, and (b) FEM-calculated geometry
Note: All dimensions are in mm

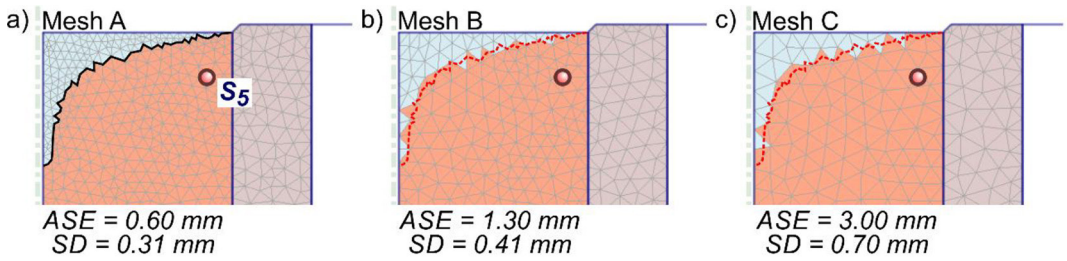

Figure 14. Effect of mesh resolution on the predicted shrinkage cavity morphology (ASE: average element size; SD: standard deviation)

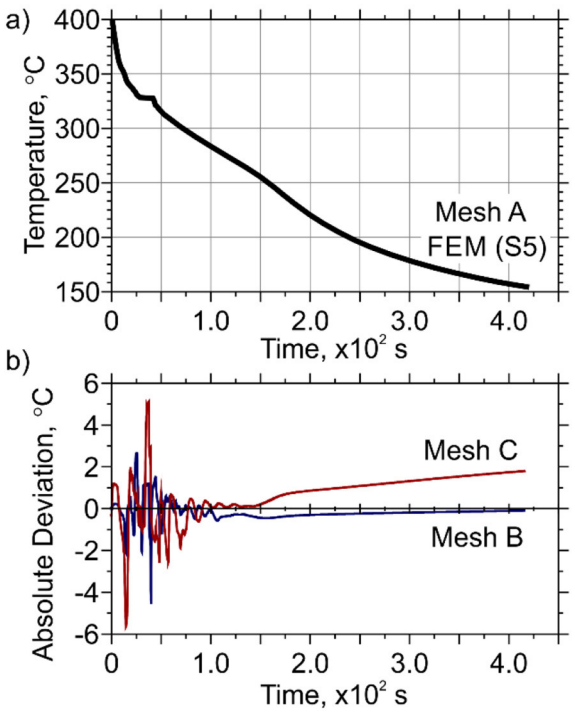

Figure 15. Temperature history at sensor 5 obtained with mesh A (a), and absolute temperature deviations for meshes B and C relative to mesh A (b)

deviation does not exceed 5.5 °C and is therefore comparable to the measurement error. The spikes in temperature deviation observed in Figure 15b are attributed to the latent heat correction algorithm. These fluctuations are localized and tend to dissipate in subsequent computational steps. However, in the case of mesh C, a persistent discrepancy is noted during the later stages of the simulation. This behavior requires further investigation and will be addressed in future research.

CONCLUSIONS

This article presents the results of a comprehensive numerical simulation concerning the solidification and cooling of a lead ingot. The simulations were performed using a proprietary FEM application developed by the author in VB.NET. The model incorporates several custom algorithms designed to accurately represent complex physical phenomena occurring during phase transition, with particular emphasis on the formation of shrinkage cavities. The primary utility of this software lies in its ability to support casting process design and predict potential defects. Although the framework also includes a mechanical module for thermal-stress analysis, the present paper primarily demonstrates the thermal-solidification and shrinkage-cavity prediction components of the methodology.

The presented results represent the culmination of extensive research aimed at developing a robust numerical tool that mirrors real-world casting processes. The study utilizes an ingot – metal mold – sand system to demonstrate the efficacy of the "multi-domain" FEM strategy. By replacing simplified surface boundary conditions with fourth-kind boundary conditions and incorporating the discrete surrounding environment, the model achieves a significantly higher degree of physical fidelity.

Furthermore, the proposed multi-domain approach validates the use of indirect temperature measurement techniques. As direct immersion of thermocouples into molten metal is often technically unfeasible and prone to signal noise, the method of embedding sensors within the surrounding molding sand has been proven to provide reliable data for model validation. These results confirm that the multi-domain FEM approach is a useful tool for characterizing heat transfer and solidification dynamics, offering a reliable alternative to traditional, highly simplified casting models.

Future research will focus on three key areas: validating the model for alloys with wider mushy

zones to better account for nonuniform solidification, conducting systematic sensitivity analysis of thermophysical properties (e.g., density, thermal resistance), and integrating the framework with experimental databases for data-assisted calibration. Ultimately, this approach will evolve the proposed methodology from a specialized tool into a comprehensive digital framework for casting process optimization.

An important direction for further development of the TGrid2D program is the full coupling of the mechanical model with the fourth-kind boundary condition. This extension would enable the model to account more accurately for dynamic cooling shrinkage, contact evolution and displacement-dependent thermal resistance in the already solidified regions of the casting.

Acknowledgements

The research was financed from the funds of the Scientific Discipline Council for Mechanical Engineering: M/KOPM/FD-20/IM-5/101.

REFERENCES

1. Seetharamu K.N., Paragasam R., Quadir G., et al. Finite element modelling of solidification phenomena. Sadhana 2001; 26(1–2): 103–120.
2. Lei C., Yang Y., Yang G., Huang Y. Magma software simulation assisted optimization of the casting system of turbocharger castings, Procedia Manufacturing 2019; 37: 59–65. https://doi.org/10.1016/j.promfg.2019.12.013
3. Campos Neto N.D., Korenyi-Both A.L., Vian C., Midson S.P., Kaufman M.J. The development of coating selection criteria to minimize die failure by soldering and erosion during aluminum high pressure die casting. Journal of Materials Processing Tech. 2023; 316: 1–24. https://doi.org/10.1016/j.jmatprotec.2023.117954
4. Dobravec T., Boštjan Mavric B, Sarler B. Improved finite difference method for phase-field modelling of dendritic solidification. Journal of Computational Physics 2026; 553: 1–21. https://doi.org/10.1016/j.jcp.2026.114716
5. Węgrzyn-Skrzypczak E. Investigation of the influence of liquid phase motion on the solidification process in the three-dimensional region. Journal of Applied Mathematics and Computational Mechanics 2021; 20(1): 103–111. https://doi.org/10.17512/jamcm.2021.1.10
6. Chaimano P., Ma N., Narasaki K., Suga T., Ren S., Kato H. Electric-thermal-mechanics modeling for in-process phenomena during micro resistance spot welding spark plug of Pt and Inconel600. Journal of Materials Research and Technology 2024; 30: 2630–2641. https://doi.org/10.1016/j.jmrt.2024.03.218
7. Pourmand S., Kermanpur A., Rezaeian A., Jafari-Ramiani A. Phase field simulation of solidification microstructure for Fe-17 wt%Cr model alloy fabricated by laser powder bed fusion. Materials & Design 2025; 260: 1–13. https://doi.org/10.1016/j.matdes.2025.115226
8. Hu M., Sun D., Zhu M. Modeling of dendrite–eutectic growth and hydrogen porosity evolution during solidification of Al–Si–Mg alloys. Journal of Materials Research and Technology 2025; 39: 6058–6069. https://doi.org/10.1016/j.jmrt.2025.10.241
9. Choudhari C.M., Narkhede B.E., Mahajan S. K. Casting design and simulation of cover plate using AutoCAST-X software for defect minimization with experimental validation. Procedia Materials Science 2014; 6: 786–797. https://doi.org/10.1016/j.mspro.2014.07.095
10. Dybowski B., Kiełbus A., Poloczek Ł. Effects of die-casting defects on the blister formation in high-pressure die-casting aluminum structural components. Engineering Failure Analysis 2023; 150: 1–15. https://doi.org/10.1016/j.engfailanal.2023.107223
11. Sowa L. Mathematical model of solidification of the axisymmetric casting while taking into account its shrinkage. Journal of Applied Mathematics and Computational Mechanics 2014; 13(4): 123–130.
12. Jia Y., Zou Q., Chen X., Le Q., Xin Y., Liu Q. Study on heat transfer behavior and process optimization in differential phase electromagnetic DC casting of extra-large AZ31B alloy flat ingot: numerical simulation and experimental verification. Journal of Materials Research and Technology 2023; 24: 1108–1131. https://doi.org/10.1016/j.jmrt.2023.03.014
13. Węgrzyn-Skrzypczak E., Skrzypczak T. Numerical modeling of the casting solidification process in a mold taking into account the influence of an air gap with variable width. Journal of Applied Mathematics and Computational Mechanics 2024; 23(2): 117–128. https://doi.org/10.17512/jamcm.2024.2.10
14. Skrzypczak T., Węgrzyn-Skrzypczak E., Sowa L. Numerical model of solidification including formation of multiple shrinkage cavities. Archives of Foundry Engineering 2020; 20(1): 37–42. https://doi.org/10.24425/afe.2020.131280
15. Skrzypczak T., Węgrzyn-Skrzypczak E., Sowa L. Numerical modeling of shrinkage cavity formation process in cast steel support. Acta Physica Polonica A 2021; 139(5): 487–490. https://doi.org/10.12693/APhysPolA.139.487
16. Węgrzyn-Skrzypczak E., Skrzypczak E. Numerical modeling of the solidification process with consideration of shrinkage cavities formation and the

influence of solid phase content on the feeding of the casting. Journal of Applied Mathematics and Computational Mechanics 2023; 22(2): 75–86. https://doi.org/10.17512/jamcm.2023.2.07

17. Jalouli Z., Caillaud A., Artozoul J., Ammar A., El-Abidi A., et al. Modelling of shrinkage formation in casting by the phase field method. International Journal of Material Forming 2021; 14 (5): 885–899. https://doi.org/10.1007/s12289-020-01602-8
18. Lewis R. W., Roberts P. M. Finite element simulation of the casting process. Applied Scientific Research 1987; 44 (1–2): 71–92. https://doi.org/10.1007/BF00384351
19. Stefanescu D. M. Science and Engineering of Casting Solidification. Springer Cham.; 2015. https://doi.org/10.1007/978-3-319-15738-2
20. Hirt C. W., Nichols B. D. Volume of fluid (VOF) method for the dynamics of free boundaries. Journal of Computational Physics 1981; 39(1): 201–225. https://doi.org/10.1016/0021-9991(81)90145-5
21. He C.-H., He J.-H. Fractal, fractional calculus, and AI: Advanced tools driving innovation in mechanical engineering. Facta Universitatis, Series: Mechanical Engineering 2026; 24(1): 1–20. https://doi.org/10.22190/FUME260218004H
22. Precup R.-E., Goanta A.-I., Roman R.-C., Hedrea E.-L. Data-driven iterative learning control of anti-windup proportional-integral fuzzy controllers for tower crane systems. Facta Universitatis, Series: Mechanical Engineering 2026; 24(1): 21–36. https://doi.org/10.22190/FUME260222007P
23. Milićević I., Popović M., Dučić N., Vujičić V., Stepanić P., Marinković D., Ćojbašić Ž. Improving the mechanical characteristics of the 3D printing objects using hybrid machine learning approach. Facta Universitatis, Series: Mechanical Engineering 2026; 24(1): 157–170. https://doi.org/10.22190/FUME220429036M
24. Majchrzak E., Mochnacki B. Numerical Methods: Theoretical Foundations, Practical Aspects, and Algorithms. Published by the Silesian University of Technology; 2004 (in Polish).
25. Belytschko T., Liu W. K., Moran B. Nonlinear Finite Elements for Continua and Structures. John Wiley & Sons; 2000.
26. Zienkiewicz O.C., Taylor R.L., Zhu J.Z. The Finite Element Method: Its Basis and Fundamentals. Elsevier Ltd.; 2013.
27. Billionnet A., Breteau J.F. A comparison of three algorithms for reducing the profile of a sparse matrix. RAIRO Opérations Research 1989; 23(3): 289–302. https://doi.org/10.1051/ro/1989230302891
28. Azad A., Jacquelin M., Buluc A., Ng E.G. The Reverse Cuthill-McKee Algorithm in Distributed-Memory. Proceedings of the 2017 IEEE International Parallel and Distributed Processing Symposium (IPDPS); 2017: 22–31. https://doi.org/10.1109/IPDPS.2017.45
29. Li D., Rong Y., Zhang B., Simić V. Assessing digital transformation capability evaluation of logistics enterprises utilizing spherical fuzzy alternative ranking order method accounting for two-step normalization approach. Facta Universitatis, Series: Mechanical Engineering 2026; 24(1): 89–116. https://doi.org/10.22190/FUME250615003L
30. Vračar L., Milovančević M., Vračar J., Matijošius J., Kilikevičius A., Buchmeister B. MQTT enabled device for industrial environment and smart city. Facta Universitatis, Series: Mechanical Engineering 2026; 24(1): 171–182. https://doi.org/10.22190/FUME200901089V
31. Brandes E. A., Brook G. B. Smithells Metals Reference Book, 7th ed. Oxford, Butterworth-Heinemann; 1998.
32. Mills K. C. Recommended Values of Thermophysical Properties for Selected Commercial Alloys. Cambridge, Woodhead Publishing; 2002.
33. Incropera F. P., DeWitt D. P., Bergman T. L., Lavine A. S. Fundamentals of Heat and Mass Transfer, 6th ed. Hoboken, John Wiley & Sons; 2007.